communications biology

A Nature Portfolio journal

Article

https://doi.org/10.1038/s42003-025-07613-y

# Cryo-EM structure of Sudan ebolavirus glycoprotein complexed with its human endosomal receptor NPC1



Fan Bu[1,2,4], Gang Ye[1,2,4], Hailey Turner-Hubbard[1,2], Morgan Herbst[1,2], Bin Liu[3] ✉ & Fang Li[1,2] ✉

Sudan ebolavirus (SUDV), like Ebola ebolavirus (EBOV), poses a significant threat to global health and security due to its high lethality. However, unlike EBOV, there are no approved vaccines or treatments for SUDV, and its structural interaction with the endosomal receptor NPC1 remains unclear. This study compares the glycoproteins of SUDV and EBOV (in their proteolytically primed forms) and their binding to human NPC1 (hNPC1). The findings reveal that the SUDV glycoprotein binds significantly more strongly to hNPC1 than the EBOV glycoprotein. Using cryo-EM, we determined the structure of the SUDV glycoprotein/hNPC1 complex, identifying four key residues in the SUDV glycoprotein that differ from those in the EBOV glycoprotein and influence hNPC1 binding: Ile79, Ala141, and Pro148 enhance binding, while Gln142 reduces it. Collectively, these residue differences account for SUDV's stronger binding affinity for hNPC1. This study provides critical insights into receptor recognition across all viruses in the ebolavirus genus, including their interactions with receptors in bats, their suspected reservoir hosts. These findings advance our understanding of ebolavirus cell entry, tissue tropism, and host range.

The ebolavirus genus, part of the filovirus family, comprises five distinct viruses, four of which are capable of infecting humans[1]. Bats are believed to be the natural reservoir for ebolaviruses, and animal-to-human transmissions have led to sporadic ebolavirus outbreaks, though no intact ebolaviruses have been isolated from bats or other animals[2,3]. Among the five ebolaviruses, Ebola virus (EBOV) is the most prevalent and has caused the highest number of human fatalities[4,5]. Sudan virus (SUDV), the second most prevalent ebolavirus, also poses a significant threat to global health and national security, having caused several recent outbreaks with a case fatality rate approaching 50%[6]. The most recent SUDV outbreaks occurred in Uganda between 2022 and 2023, resulting in 164 cases[7]. This outbreak highlights our ongoing vulnerability, as there is currently no FDA-approved vaccine or therapeutic for SUDV, unlike EBOV. Research on SUDV has been relatively limited, particularly in understanding its receptor recognition and cell entry mechanisms, which are crucial for evaluating its infectivity, tissue tropism, and host range, and for developing vaccines and treatments[8]. This study aims to address these gaps through a combination of structural biology, biochemistry, and sequence analysis.

The glycoprotein (GP) of ebolaviruses guides viral entry into host cells[9]. It assembles as a homotrimer on the virus surface, consisting of three copies each of the receptor-binding subunit GP1 and the membrane-fusion subunit GP2[10]. During maturation, the trimeric GP is cleaved at the GP1/GP2 junction by the protease furin, but GP1 and GP2 remain connected through a disulfide bond and noncovalent interactions. Each GP1 subunit contains a receptor-binding site (RBS), which is initially covered by a glycan cap and a mucin-like domain (MLD)[9,11]. To enable entry, GP1 first attaches to non-specific cell-surface factors, allowing the virus to be internalized via endocytosis[12]. Once inside the endosomes, endosomal proteases remove the glycan cap and MLD, resulting in GPcl (the cleaved form of GP) and exposing the RBS[13]. The exposed RBS then binds to Niemann-Pick C1 (NPC1), the ebolavirus receptor on the endosomal membrane[14–16]. Following this, GP2 undergoes dramatic conformational changes, fusing the viral and endosomal membranes to release the viral genome into the host cell's cytoplasm[17,18].

NPC1 serves as the endosomal receptor for ebolaviruses and is essential for viral entry into cells[14–16]. This transmembrane protein is widely expressed throughout the human body and is predominantly localized in late endosomes and lysosomes. A previous study resolved the cryo-EM structure of EBOV GPcl complexed with full-length human NPC1, demonstrating that the second luminal domain of NPC1, known as Domain C (NPC1-C), is responsible for binding filoviruses[15]. Another study determined the crystal structure of EBOV GPcl bound to NPC1-C, revealing that NPC1-C interacts with the receptor-binding site (RBS) of EBOV GPcl, located in a hydrophobic pocket, through two protruding loops - Loop 1 and Loop 2[16]. Interestingly, the binding affinity between NPC1-C and EBOV GPcl is

[1]Department of Pharmacology, University of Minnesota Medical School, Minneapolis, MN, USA. [2]Center for Emerging Viruses, University of Minnesota, Minneapolis, MN, USA. [3]Hormel Institute, University of Minnesota, Austin, MN, USA. [4]These authors contributed equally: Fan Bu, Gang Ye.
✉e-mail: liu00794@umn.edu; lifang@umn.edu

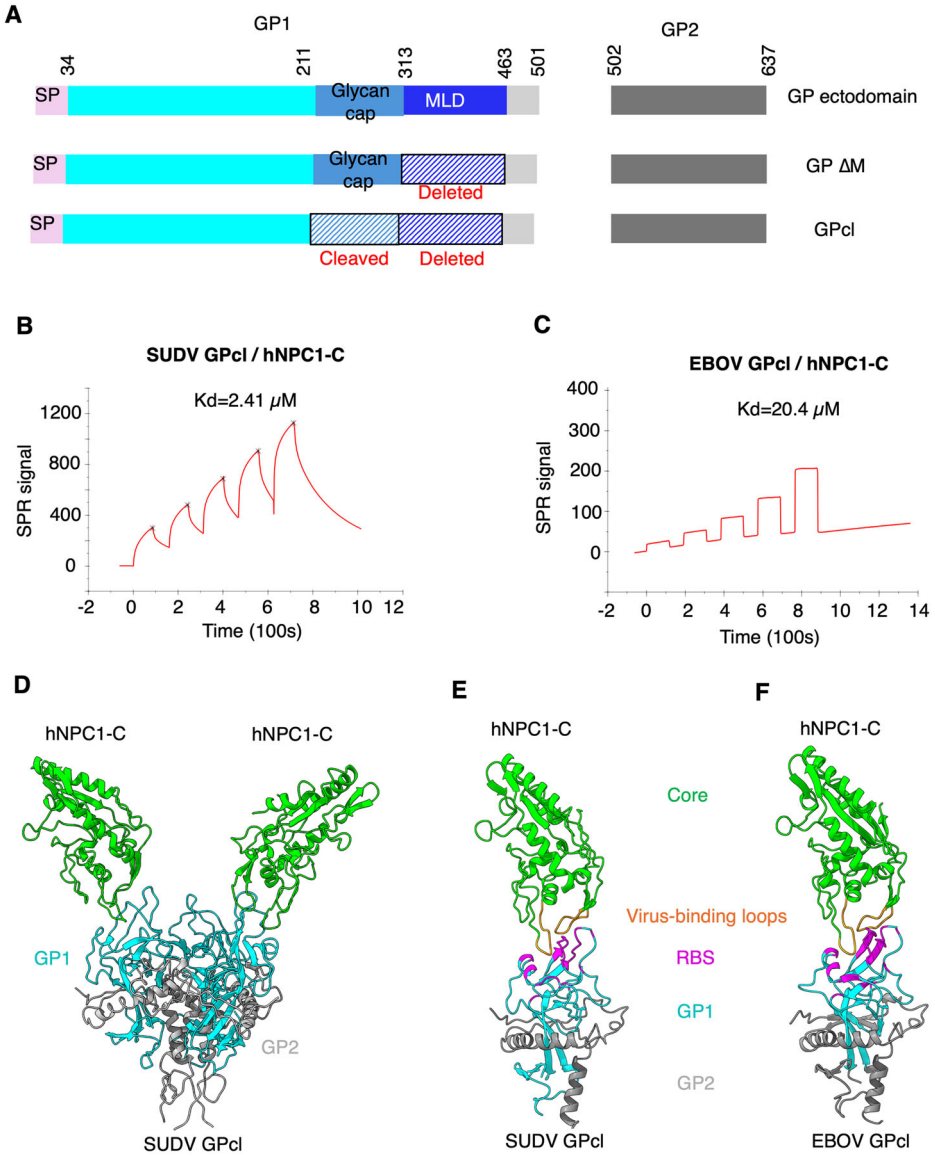


**Fig. 1 | Overall structural interactions between SUDV GP and its endosomal receptor, human NPC1. A** Schematic representations of three versions of SUDV GP: GP ectodomain, GP ΔM, and GPcl. GP1 represents the receptor-binding subunit, and GP2 is the membrane-fusion subunit. MLD refers to the mucin-like domain. **B** Binding affinity between SUDV GPcl and hNPC1-C (Domain C of human NPC1) measured using surface plasmon resonance (SPR). Recombinant GPcl was immobilized on a CM5 sensor chip via chemical cross-linking, and recombinant hNPC1-C was injected at various concentrations. Data were analyzed using Biacore Evaluation Software. **C** Binding affinity between EBOV GPcl and hNPC1-C measured under conditions similar to (**B**) using SPR. **D** Overall structure of the SUDV GPcl in complex with hNPC1-C, determined by cryo-EM. SUDV GPcl forms a trimer, with two of the three protomers bound by hNPC1-C. hNPC1-C is shown in green, GP1 in cyan, and GP2 in gray. **E** Structure of a single SUDV GP protomer bound to hNPC1-C. **F** Previously determined crystal structure of a single EBOV GP protomer bound to hNPC1-C (PDB: 5F1B). The two virus-binding loops in hNPC1-C and the receptor-binding site (RBS) in the viral GP are shown in orange and magenta, respectively.

relatively weak, with a dissociation constant (Kd) of about 100 μM[16], much weaker than the binding affinities of receptors for other viruses, such as coronaviruses, which bind in the nanomolar range[19–22]. This raises questions about how efficiently EBOV can infect tissues with low NPC1 expression. The structural interaction between SUDV and NPC1 has not yet been experimentally characterized. Additionally, the impact of sequence variations among different ebolaviruses on their binding affinity to human NPC1 remains unknown, limiting our understanding of receptor recognition and cell entry mechanisms for other ebolaviruses. Furthermore, it is unclear how genetic variations in NPC1 across different host species affect the host range of ebolaviruses. Previous studies have shown that NPC1 from African straw-colored fruit bats (Eidolon helvum) is recognized by SUDV, but only poorly by EBOV, due to a single amino acid difference between human NPC1 and that of E. helvum bats[23]. The molecular mechanism behind this observation is not yet understood. Therefore, understanding the structural interaction between SUDV GP and NPC1 is crucial for better insights into receptor recognition, cell entry, tissue tropism, and host range of not only SUDV but also other ebolaviruses.

In this study, we compared the binding affinities of SUDV GPcl and EBOV GPcl to human NPC1-C and determined the structure of the SUDV GPcl complexed with human NPC1-C, the first such structure to our knowledge. From this structure, we identified key residue differences between SUDV and EBOV GPs that influence their differential binding to human NPC1. Biochemical studies were performed to validate our structural findings. Using these insights, we analyzed GP sequences from various ebolaviruses and examined sequence variations between human and bat NPC1. Collectively, these analyses provide a deeper understanding of receptor recognition, cell entry, tissue tropism, and host range across the ebolavirus genus.

## Results

### Binding of SUDV GPcl to human NPC1

To investigate the interaction between SUDV GP and human NPC1 (hNPC1), we expressed and purified a version of the SUDV GP ectodomain lacking the mucin-like domain (MLD), which we designated as SUDV GP-ΔM (Fig. 1A). Similarly, we expressed and purified EBOV GP-ΔM, using the same design as for SUDV GP-ΔM. We also prepared Domain C of hNPC1, referred to as hNPC1-C. To evaluate the binding between SUDV GP and hNPC1-C, we removed the glycan cap from both SUDV GP-ΔM and EBOV GP-ΔM through proteolysis, producing SUDV GPcl and EBOV GPcl, respectively (Fig. 1A). These GPcl proteins represent the primed, receptor-binding forms of ebolavirus GPs and are the main focus of this study. We then measured the binding affinity between the two GPcls and hNPC1-C using surface plasmon resonance (SPR). The results indicated that SUDV GPcl and EBOV GPcl bind to hNPC1-C with dissociation constants (Kd) of 2.41 μM and 20.4 μM, respectively (Fig. 1B, C). Thus, SUDV GPcl binds to hNPC1-C approximately nine times more strongly than EBOV GPcl.

**Table 1 | Cryo-EM data collection, refinement, and validation statistics**

| | SUDV GPcl / hNPC1-C (PDB 9DZ2) (EMD-47323) |
|---|---|
| **Data collection and processing** | |
| Magnification | 130,000 |
| Voltage (kV) | 300 |
| Electron exposure (e–/Å$^2$) | 53.7 |
| Defocus range (μm) | −1.0 ~ −2.0 |
| Pixel size (Å) | 0.664 |
| Symmetry imposed | C1 |
| Initial particle images (no.) | 656,688 |
| Final particle images (no.) | 159,976 |
| Map resolution (Å) | 3.31 |
| FSC threshold | 0.143 |
| Map resolution range (Å) | 2.8–5.2 |
| **Refinement** | |
| Initial model used (PDB code) | 5f1b |
| Model resolution (Å) | 3.10 |
| FSC threshold | 0.5 |
| Map sharpening *B* factor (Å$^2$) | −112.6 |
| Model composition | |
| Non-hydrogen atoms | 9523 |
| Protein residues | 1207 |
| *B* factors (Å$^2$) | |
| Protein | 70.17 |
| R.m.s. deviations | |
| Bond lengths (Å) | 0.004 |
| Bond angles (°) | 0.739 |
| **Validation** | |
| MolProbity score | 1.97 |
| Clashscore | 10.10 |
| Poor rotamers (%) | 0.49 |
| Ramachandran plot | |
| Favored (%) | 93.15 |
| Allowed (%) | 6.26 |
| Disallowed (%) | 0.59 |

### Structure of SUDV GPcl complexed with human NPC1

To examine the structural interaction between SUDV GP and hNPC1, we determined the cryo-EM structure of the SUDV GPcl complexed with hNPC1-C. The structure was refined to a resolution of 3.31 Å (Table 1; Supplementary Fig. 1), revealing a trimeric SUDV GPcl bound by two copies of hNPC1-C (Fig. 1D). The trimeric SUDV GPcl consists of three GP1 subunits, each lacking the MDL and glycan cap, and a trimeric GP2 stalk. The receptor-binding site (RBS) is located in a cavity at the top of the truncated GP1, with hNPC1-C sitting on top of it (Fig. 1D, E). When comparing our cryo-EM structure of the SUDV GPcl/hNPC1-C complex with the crystal structure of the EBOV/hNPC1-C complex, we observed that the overall binding modes of the two complexes are similar (Fig. 1E, F). For each monomeric SUDV GPcl/hNPC1-C complex, two loops in hNPC1 interact with the RBS of SUDV GPcl (Fig. 2A). Loop 1 rests on the surface of the RBS, while Loop 2 inserts into the cavity of the RBS. The cryo-EM density map clarified the detailed interactions between SUDV GPcl and hNPC1-C (Supplementary Fig. 2). In total, 9 residues in hNPC1-C Loop 1, 8 residues in hNPC1-C Loop 2, and 16 residues in the SUDV RBS are involved in the binding interactions (Fig. 2A, B). Among these 16 residues in the SUDV RBS, only four differ from the EBOV RBS: residues 79, 141, 142, and 148. Of these, residue 142 interacts with Loop 1 and residues 79, 141 and 148 interact with Loop 2 (Fig. 2A, B). Therefore, these four residue differences are responsible for the stronger binding of SUDV GPcl to hNPC1 compared to EBOV GPcl.

The most notable difference between the SUDV RBS/hNPC1-C and EBOV RBS/hNPC1-C interfaces is the significant conformational change in Loop 1 of hNPC1-C. At the SUDV RBS/hNPC1-C interface, Loop 1 has shifted >6 Å away from the RBS compared to its position at the EBOV RBS/hNPC1-C interface (Fig. 3A; Supplementary Fig. 3). This shift is mainly driven by the S142Q residue change in the SUDV RBS, where Gln142, with its larger side chain, pushes Loop 1 away from the RBS. As a result, at the EBOV RBS/hNPC1-C interface, the main chains of residues 141-143 in the RBS form stacking interactions with residues 424-427 in hNPC1-C (Fig. 3B). In contrast, at the SUDV RBS/hNPC1-C interface, these main chain stacking interactions no longer exist due to the conformational shift in Loop 1, caused by Gln142 (Fig. 3C). This makes Gln142 in SUDV RBS less favorable for hNPC1-C binding compared to Ser142 in EBOV RBS.

Although Loop 2 of hNPC1-C adopts a similar conformation at both the SUDV RBS/hNPC1-C and EBOV RBS/hNPC1-C interfaces, the specific interactions differ due to variations in the residues between the two RBS regions. At the EBOV RBS/hNPC1-C interface, Ala148 from the RBS does not interact with hNPC1-C (Fig. 4A). However, at the SUDV RBS/hNPC1-C interface, Pro148 forms a hydrophobic stacking interaction with the side chain of Asp502 from hNPC1-C (Fig. 4B). The A148P residue change from EBOV RBS to SUDV RBS enhances hNPC1-C binding by introducing this favorable hydrophobic stacking interaction. At the EBOV RBS/hNPC1-C interface, the polar hydroxyl group of Tyr423 from hNPC1-C forms unfavorable interactions with the hydrophobic side chains of Val79 and Val141 from the RBS (Fig. 4C). In contrast, at the SUDV RBS/hNPC1-C interface, Ala141, with its smaller hydrophobic side chain compared to valine, stays farther from the polar hydroxyl group of Tyr423 from hNPC1-C (Fig. 4D). Additionally, Ala141 is stabilized by a favorable hydrophobic interaction with Ile79 from the RBS, which is not possible with valine due to its shorter side chain compared to isoleucine. Thus, the V141A and V79I residue changes from EBOV RBS to SUDV RBS improve hNPC1-C binding by alleviating an unfavorable interaction and creating a new favorable interaction at the RBS/hNPC1-C interface. Overall, Pro148, Ala141, and Ile79 in the SUDV RBS are more conducive to hNPC1-C binding compared to Ala148, Val141, and Val79 in the EBOV RBS, respectively.

### Biochemical validation of structural data

To validate the structural data, we performed two biochemical assays to evaluate how residue differences between the SUDV and EBOV RBS regions affect viral receptor binding and viral entry. First, we conducted SPR experiments between hNPC1-C and several SUDV GPcl variants, each containing a mutation corresponding to a residue change from the SUDV RBS to the EBOV RBS: I79V, A141V, Q142S, and P148A (Supplementary Figs. 4, 5). Additionally, we included a variant of SUDV GPcl with an A141V/Q142S/P148A triple mutation, as these residues are located near one another. The results showed that the I79V, A141V, and P148A mutations reduced SUDV GPcl's binding affinity to hNPC1-C, while the Q142S mutation increased the binding affinity (Fig. 5A; Supplementary Fig. 6; Supplementary Data 1). Furthermore, the A141V/Q142S/P148A triple mutation also reduced SUDV GPcl's binding affinity to hNPC1-C. Second, we conducted a SUDV pseudovirus entry assay using SUDV GPcl containing the same mutations (Fig. 5B; Supplementary Figs. 7, 8). Lentiviruses pseudotyped with SUDV GPcl were used to enter hNPC1-expressing human cells. The results indicated that the I79V, A141V, and A141V/Q142S/P148A mutations reduced SUDV pseudovirus entry, whereas the Q142S mutation enhanced entry. The P148A mutation exhibited a trend toward reducing SUDV pseudovirus entry, though the result was not statistically significant. Overall, these biochemical assays align with the structural data, showing that residue differences between SUDV and EBOV GPcl generally favor SUDV GPcl's binding to hNPC1, with the exception of residue 142.

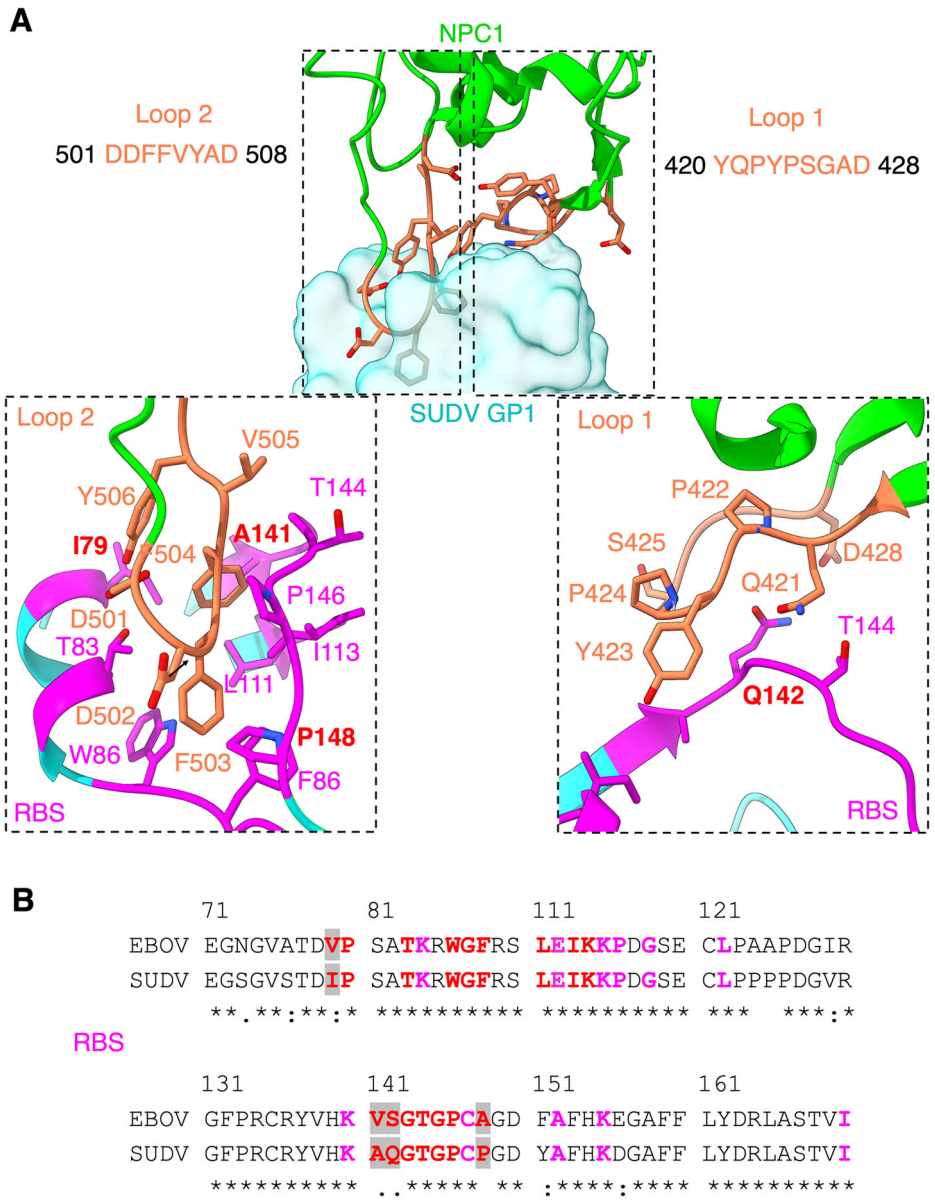


**Fig. 2 | Detailed structural interactions between SUDV GP and hNPC1. A** Interface between SUDV GPcl and hNPC1-C. hNPC1-C interacts with SUDV GPcl through two loops. Top panel: Residues of the two receptor loops are shown as orange sticks, while the RBS of SUDV GPcl is displayed as a cyan surface. Bottom panels: Residues of the two receptor loops are shown as orange sticks, and receptor-contacting residues within the RBS are shown as magenta sticks. Four receptor-contacting residues that differ between the RBS regions of SUDV and EBOV are highlighted in red. **B** Sequence alignment of the RBS regions between EBOV and SUDV. RBS residues are shown in magenta, with receptor-contacting residues highlighted in red. The four receptor-contacting residues that differ between SUDV and EBOV are shaded. Fully conserved residues are indicated with asterisks (*), strongly conserved residues with colons (:), and weakly conserved residues with periods (.).

## Discussion

SUDV is a highly lethal virus with no approved drugs or vaccines currently available as countermeasures. A significant gap in SUDV research is that its receptor binding and cell entry mechanisms are not as well understood as those of EBOV. Viruses in the ebolavirus genus use a unique cell entry mechanism: the RBS of their GP is initially covered by the glycan cap and MLD, which only becomes exposed in endosomes after endosomal proteases cleave off these structures. At that point, the GP binds to its NPC1 receptor on the endosomal membranes, enabling the viruses to penetrate the endosomal membrane. Therefore, the interaction between ebolavirus GPcl (the cleaved form of GP) and NPC1 is presumed to be a key factor influencing cell entry efficiency, tissue tropism, and host range.

In this study, we discovered that SUDV GPcl binds to human NPC1 approximately nine times more strongly than EBOV GPcl. Among the receptor-contacting residues in the RBS region, only four (residues 79, 141, 142, and 148) differ between SUDV GPcl and EBOV GPcl, indicating that these four residues are the key determinants of SUDV GPcl's stronger receptor-binding affinity. We determined the cryo-EM structure of the SUDV GPcl bound to hNPC1-C (Domain C of hNPC1), revealing the structural role of each of these four RBS residue changes in hNPC1-C binding. Among these, Ile79, Ala141, and Pro148 in SUDV GPcl are more favorable for hNPC1-C binding than Val79, Val141, and Ser142 in EBOV GPcl, respectively, while Gln142 in SUDV GPcl is less favorable for hNPC1-C binding than Ser142 in EBOV GPcl. We confirmed the structural findings with biochemical assays. Together, these data suggest that the relatively high NPC1-C-binding affinity of SUDV GPcl could facilitate the virus's entry into cells, potentially allowing SUDV to infect tissues with lower NPC1 expression, such as the respiratory system, gastrointestinal tract, muscles, connective and soft tissues, and skin[24]. This elevated binding affinity also implies that entry inhibitors targeting the RBS of SUDV would need to counteract its stronger receptor interaction. It is important to note that other factors also contribute to viral infectivity and tissue tropism, and this study focuses specifically on receptor binding, which is just one of these determinants.

Our study advances the understanding of receptor binding in the ebolavirus genus, for which structural interactions with human NPC1 are unavailable for three of the viruses. We analyzed the RBS region sequences from all five ebolaviruses and found that only the four residues examined in this study have undergone variations across these viruses (Fig. 6A). At positions 79 and 141, SUDV is the only virus that contains Ile79 and Ala141, while the other four viruses have Val79 and Val141. As demonstrated in our study, Ile79 and Ala141 are more favorable for hNPC1-C binding than Val79 and Val141, respectively. At position 142, both SUDV and RESTV have Gln142,

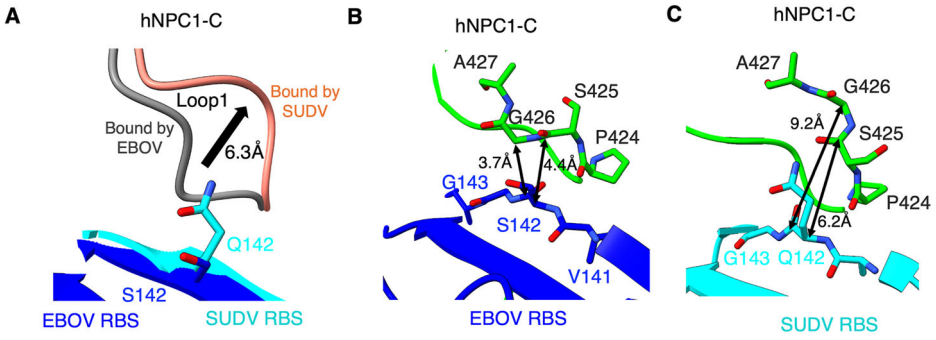


**Fig. 3 | Detailed structural interactions between the SUDV RBS and Loop 1 of hNPC1-C. A** A significant conformational change in Loop 1 of hNPC1-C is observed when bound to SUDV compared to EBOV. This shift involves Loop 1 moving 6.3 Å away from the RBS, driven by the presence of Q142 in the SUDV RBS. **B** Detailed interactions between the EBOV RBS and Loop 1 of hNPC1-C. **C** Detailed interactions between the SUDV RBS and Loop 1 of hNPC1-C. Double arrows in (**B**) indicate hydrophobic stacking interactions, whereas in (**C**), the distances are too great to support such hydrophobic stacking interactions.

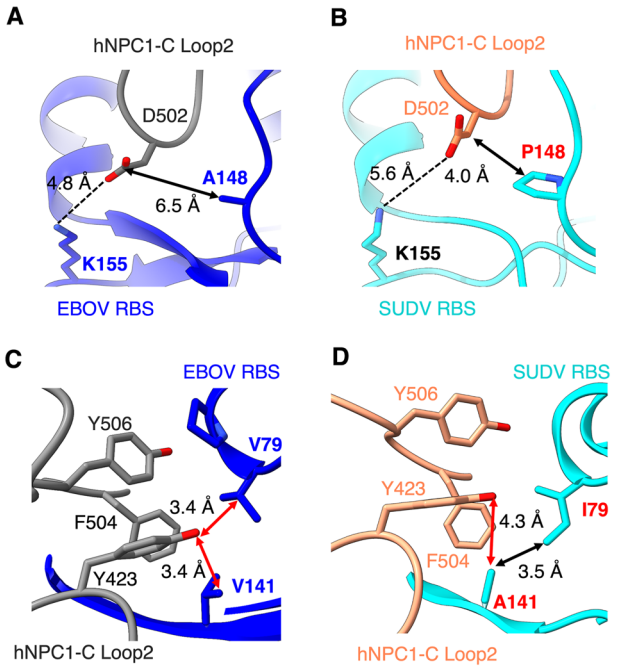


**Fig. 4 | Detailed structural interactions between the SUDV RBS and Loop 2 of hNPC1-C. A** Interactions between Ala148/Lys155 in the EBOV RBS and Loop 2 of hNPC1-C. **B** Interactions between Pro148/Lys155 in the SUDV RBS and Loop 2 of hNPC1-C. A dotted line in (**A**) indicates a long-range salt bridge, which is absent in (B) due to the greater distance. The double arrow in (**B**) represents a hydrophobic interaction that cannot form in (**A**) because of the larger distance. **C** Interactions between Val79/Val141 in the EBOV RBS and Loop 2 of hNPC1-C. **D** Interactions between Ile79/Ala141 in the SUDV RBS and Loop 2 of hNPC1-C. In (**C**), red double arrows indicate unfavorable interactions between a polar functional group and hydrophobic functional groups. In (**D**), the distance is sufficient to alleviate these unfavorable interactions, and the black double arrow highlights a favorable hydrophobic interaction.

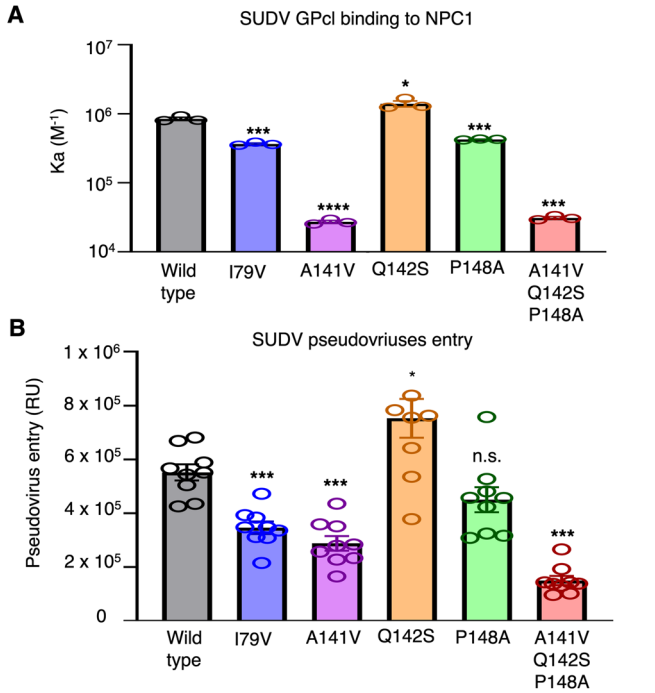


**Fig. 5 | Biochemical assays investigating the effects of residue changes from the SUDV RBS to the EBOV RBS on receptor binding and viral entry. A** SPR assay evaluating the binding of SUDV GPcl (wild type and variants) to hNPC1-C. Each SUDV GPcl variant includes mutations corresponding to residue changes from the SUDV RBS to the EBOV RBS. In the SPR assay, GPcl was immobilized on a sensor chip via chemical crosslinking, and hNPC1-C was injected over the chip. Data are shown as mean ± SEM ($n = 3$). Statistical differences between wild-type GPcl and each variant were analyzed using a Student's two-tailed t-test, with significance levels indicated above each bar: $^{****}P < 0.001$; $^{***}P < 0.001$; $^{*}P < 0.05$. **B** SUDV pseudovirus entry assay assessing the entry efficiency of SUDV pseudoviruses (wild type and variants) into human cells expressing hNPC1. Each SUDV pseudovirus variant includes mutations corresponding to residue changes from the SUDV RBS to the EBOV RBS. Before the assay, all pseudoviruses were treated with protease to remove the MLD and glycan cap. Pseudovirus entry signals were normalized based on GP expression levels on each pseudovirus. Data are presented as mean ± SEM ($n = 9$). Statistical differences between the wild type and each mutant were analyzed using a Student's two-tailed *t*-test, with significance levels indicated above each bar: $^{***}P < 0.001$; $^{*}P < 0.05$; n.s., not statistically significant.

while the other three viruses have Ser142. Our data show that Ser142 is more favorable for hNPC1 binding than Gln142. At position 148, only EBOV contains Ala148, while the other four viruses have Pro148, which, as we demonstrated, is more favorable for hNPC1 binding than Ala148. Notably, the A141V substitution has the most significant impact on hNPC1-C binding. Overall, SUDV possesses three favorable residues (including the critical Ala141) and one unfavorable residue. In contrast, EBOV, BDBV, and TAFV each have one favorable residue and three unfavorable ones (including the critical Val141), while RESTV has all four unfavorable residues (including the critical Val141). Based on hNPC1-C binding affinity, SUDV ranks the highest, followed by EBOV, BDBV, and TAFV, with RESTV ranking last. This could potentially explain the lack of pathogenicity in humans for RESTV infections[25]. However, it is important to note that ebolavirus pathogenesis is a complex process, influenced by numerous factors beyond the RBS/hNPC1 interaction. Therefore, the findings from this analysis require experimental validation and should be considered as just one of several factors that contribute to ebolavirus pathogenesis.

The animal origins and host ranges of ebolaviruses have been a subject of significant interest. Although bats are believed to be the natural reservoir for ebolaviruses, infectious ebolaviruses have yet to be isolated from bats. Previous research has shown that NPC1 from the bat species E. helvum is poorly

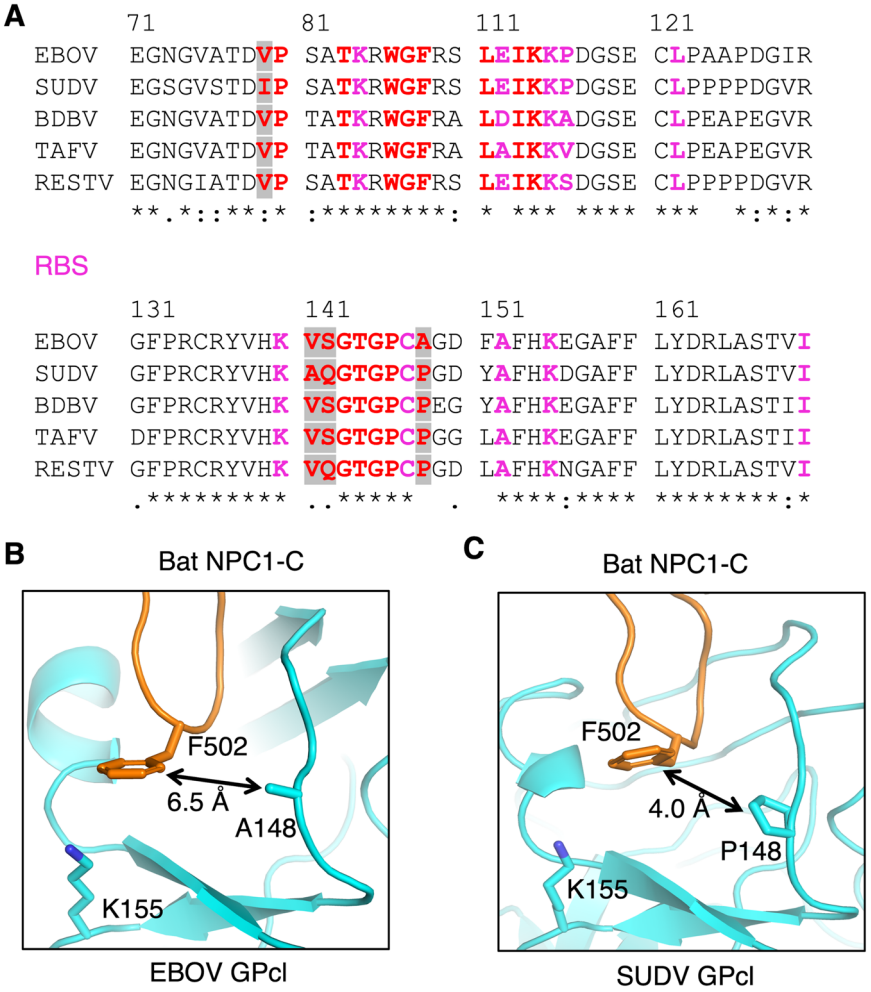


**Fig. 6 | Structural data used to assess human receptor binding by various ebolaviruses and bat receptor binding by SUDV and EBOV. A** Sequence alignment of receptor-binding site (RBS) regions in ebolavirus glycoproteins (GPs). Residues are colored as shown in Fig. 2B. **B** Structural model of bat NPC1-C bound to EBOV GPcl. **C** Structural model of bat NPC1-C bound to SUDV GPcl. A D502F mutation was introduced in both (**B**) and (**C**) using PyMOL modeling[37].

recognized by EBOV GPcl[23]. This poor recognition is likely due to positive selection in bat NPC1, possibly as an evolutionary adaptation to evade EBOV infections. This restriction has been linked to a single residue change in bat NPC1, where Glu502 in human NPC1 is replaced by phenylalanine in bat NPC1. Studies have also revealed that a single mutation in EBOV GPcl, V141A, can overcome this restriction, allowing EBOV GPcl to bind to bat NPC1[23]. The molecular mechanisms behind these findings were previously unclear. Building on our discoveries, we examined the residue change at position 502 in bat NPC1. As suggested by previous studies, at the EBOV RBS/human NPC1 interface, Asp502 in hNPC1 forms a long-range salt bridge with Lys155 in the EBOV RBS (Fig. 4A)[16]. However, at the EBOV RBS/bat NPC1 interface, Phe502 in bat NPC1 cannot form this salt bridge with Lys155 in the EBOV RBS (Fig. 6B), explaining why EBOV GPcl cannot bind to bat NPC1. At the SUDV RBS/bat NPC1 interface, Phe502 in bat NPC1 can form a hydrophobic interaction with Pro148 in SUDV RBS (Fig. 6C). This analysis suggests that the D502F residue change from human to bat NPC1 may result from positive selection in bat NPC1 to evade EBOV, but not SUDV. Indeed, previous studies have shown that NPC1 from E. helvum bats can be recognized by SUDV GPcl[23]. Additionally, as demonstrated in this study, the V141A mutation enhances the binding between the RBS and NPC1-C by eliminating an unfavorable interaction at the binding interface. Thus, the V141A mutation may compensate for the loss of the salt bridge between Phe502 in bat NPC1 and Lys155 in the RBS, lifting the restriction on EBOV infection in bat cells. Therefore, our study provides a molecular explanation for previous findings on the potential host range of ebolaviruses.

In summary, the implications of this study go beyond the receptor binding, cell entry, tissue tropism, and host range of SUDV, as it also enhances our broader understanding of ebolaviruses.

## Methods

### Cell lines and plasmids

HEK293T cells (American Type Culture Collection, ATCC) were maintained in Dulbecco's Modified Eagle Medium (DMEM) supplemented with 10% fetal bovine serum, 2 mM L-glutamine, 100 units/mL penicillin, and 100 μg/mL streptomycin. Expi293F cells (ThermoFisher) used for protein expression were cultured in Expi293 Expression Medium (ThermoFisher). No commonly misidentified cell lines were used in this study.

The genes for SUDV GP (NCBI Reference Sequence: NC_006432.1), EBOV GP (NCBI Reference Sequence: NC_002549.1), and human NPC1 (UniProt: O15118) were synthesized by GenScript. For pseudovirus production, the full-length SUDV GP gene was cloned into the pcDNA3.1(+) vector with a C-terminal C9 tag. For protein expression, the genes encoding EBOV GP-ΔM (residues 1–632, excluding residues 312–464 for the MLD) and SUDV GP-ΔM (residues 1–637, excluding residues 312–464 for the MLD) were cloned into the Lenti-CMV vector (Vigene Biosciences) with a C-terminal foldon trimerization motif followed by a His tag. The human NPC1-C gene (residues 374–620) was cloned into the same vector with a tPA signal peptide at the N-terminus and a Strep-tag II at the C-terminus.

### Protein expression and purification

Plasmids encoding EBOV GP-ΔM, SUDV GP-ΔM, and human NPC1-C were transiently transfected into Expi293F cells using polyethylenimine (PEI, Polysciences). Three days post-transfection, the supernatants were collected. GP-ΔM proteins were purified using a Ni-NTA column (Cytiva), followed by further purification on a Superose200 gel filtration column (Cytiva). To generate GPcl, 1 mg of GP-ΔM was digested with 5 μg of thermolysin L (Sigma-Aldrich) at room temperature overnight and

subsequently purified using a Superose200 gel filtration column (Cytiva). Human NPC1-C protein was purified using a Strep-Tactin XT column (Cytiva) and further refined with a Superose200 gel filtration column.

### Surface plasmon resonance

Surface plasmon resonance (SPR) was used to measure the binding affinity between recombinant GPcl (from EBOV or SUDV) and recombinant human NPC1-C using the Biacore S200 system (Cytiva), as previously described[26,27]. Recombinant GPcl was immobilized on a CM5 sensor chip (Cytiva) via chemical crosslinking. Human NPC1-C was injected at varying concentrations (1.25 μM to 20 μM) in a running buffer containing 50 mM MES (pH 6.0), 150 mM NaCl, and 0.05% Tween20. The resulting data were analyzed using Biacore Evaluation Software (Cytiva).

### Pseudovirus cell entry assay

A pseudovirus entry assay was performed to assess the entry efficiency of SUDV pseudoviruses, as previously described[28,29]. SUDV pseudoviruses were generated by co-transfecting HEK293T cells with a pcDNA3.1(+) plasmid encoding full-length SUDV GP, a helper plasmid psPAX2 encoding the HIV backbone, and a reporter plasmid plenti-CMV-luc. After 72 hours, the SUDV pseudoviruses were harvested, and their GP was cleaved into GPcl by treating with 1 mg/mL freshly prepared thermolysin L in the presence of 2 mM CaCl2, followed by a 30-minute incubation at 37 °C. The reaction was halted by adding 500 μM phosphoramidon. The cleaved SUDV pseudoviruses (GPcl pseudoviruses) were then used to infect 293 T cells transiently expressing full-length human NPC1. After 48 hours, the cells were lysed, and portions of the lysates were transferred to new plates. Luciferase substrate was added, and Relative Light Units (RLUs) were measured using an EnSpire plate reader (PerkinElmer).

### Cryo-EM data collection

SUDV GPcl and human NPC1-C were mixed at a molar ratio of 1:4 and diluted to a concentration of 0.3 mg/mL. A 4 μL aliquot of the mixture was applied to freshly glow-discharged Quantifoil R1.2/1.3 300-mesh copper grids (Electron Microscopy Sciences), blotted for 4 seconds at 22 °C under 100% humidity, and plunge-frozen in liquid ethane using a Vitrobot Mark IV (FEI). Images were captured using a K3 Summit detector (Gatan) with a BioQuantum GIF energy filter (20 eV slit width) in CDS mode, attached to a 300 kV FEI Titan-Krios TEM at the Hormel Institute, University of Minnesota. Data collection was performed with EPU software (ThermoFisher Scientific) at a pixel size of 0.664 Å (nominal magnification 130,000x) and a defocus range of −1.0 to −2.0 μm. Each image consisted of 40 dose-framed fractions, recorded with a total electron dose of 53.7 e-/Å$^2$. Cryo-EM data collection statistics are summarized in Table 1.

### Cryo-EM data processing, model building and refinement

Cryo-EM data were processed using cryoSPARC v4.5.1[30], following the workflow detailed in Supplementary Fig. 1. A total of 15,337 dose-fractionated movies were motion-corrected using MotionCor2[31], and contrast transfer function (CTF) estimation was performed with CTFFIND-4.1.13[32]. The data were downsampled to 0.885 Å/pixel. Images with defocus values outside the range of −0.6 to −3.2 μm or with CTF fits worse than 7 Å were excluded. A total of 9,526,509 particles were selected using the Blob and Template pickers in cryoSPARC v4.5.1. Three rounds of 2D classification were performed to remove junk particles, resulting in 656,688 particles for Ab-initio reconstruction of four maps, followed by heterogeneous refinement. Two rounds of 3D classification yielded 159,976 particles, which were subjected to non-uniform and CTF refinement, producing a final map at 3.31 Å resolution. Post-processing with the Cryo-EM Feature Enhancement Model[33] further improved map density. The final resolution was calculated using gold-standard Fourier shell correlation (FSC) at a cutoff of 0.143 between the two half-maps. Local resolution estimates were obtained using cryoSPARC v4.5.1.

Initial model building of the SUDV GPcl/human NPC1-C complex was performed in Coot-0.8.9[34], using 5F1B as the starting model. Refinement was carried out using Phenix-1.16[35] alongside manual adjustments in Coot-0.8.9. Within the SUDV GPcl trimer, two of the three subunits were occupied by human NPC1-C. To confirm the binding of two hNPC1-C molecules to the trimeric SUDV GPcl, additional 3D classification of the particles was performed, revealing no complexes with full occupancy (i.e., three hNPC1-C receptors bound). Applying C3 symmetry resulted in lower map resolution, further supporting the absence of a threefold axis of symmetry. Of the two bound NPC1-C molecules, the better-resolved one was selected for atomic model building. Model and map statistics are summarized in Table 1. Figures were prepared using UCSF Chimera X v0.93[36] and the PyMOL Molecular Graphics System, Version 3.0[37]. Contact residues between SUDV GP and human NPC1-C were identified using LigPlot[38].

### Statistics and reproducibility

Data analysis and statistical assessments for the pseudovirus entry assay and protein-protein binding affinity measurements were conducted using GraphPad Prism (version 10.3.0). The pseudovirus entry assay was performed with nine replicates, utilizing the same batch of pseudoviruses to infect an equal number of cells seeded in separate wells. Protein-protein binding affinity measurements were performed in triplicate. The Ka values were calculated using surface plasmon resonance (SPR) with the same batch of GPcl and NPC1-C proteins, with each Ka value obtained from independent injections. Statistical analyses were conducted using unpaired two-tailed Student's t-tests to determine the significance of differences between mutants (proteins or pseudoviruses) and wild-type controls. All cryo-EM-related statistics are summarized in Table 1.

### Reporting summary

Further information on research design is available in the Nature Portfolio Reporting Summary linked to this article.

## Data availability

The atomic model and corresponding cryo-EM density map for Sudan ebolavirus GP complexed with human NPC1 have been deposited into the PDB and the Electron Microscopy Data Bank, respectively, with accession numbers 9DZ2 and EMDB-47323. All other data are available from the corresponding authors on reasonable request.

Received: 21 November 2024; Accepted: 28 January 2025;
Published online: 02 February 2025

## References

1. Kuhn, J. H. et al. ICTV Virus Taxonomy Profile: Filoviridae. *J. Gen. Virol.* **100**, 911–912 (2019).
2. Leroy, E. M. et al. Fruit bats as reservoirs of Ebola virus. *Nature* **438**, 575–576 (2005).
3. Leroy, E. M. et al. Human Ebola outbreak resulting from direct exposure to fruit bats in Luebo, Democratic Republic of Congo, 2007. *Vector Borne Zoonotic Dis.* **9**, 723–728 (2009).
4. Jacob, S. T. et al. Ebola virus disease. *Nat. Rev. Dis. Prim.* **6**, 13 (2020).
5. Leroy, E. M., Labouba, I., Maganga, G. D. & Berthet, N. Ebola in West Africa: the outbreak able to change many things. *Clin. Microbiol Infect.* **20**, O597–O599 (2014).
6. Lefebvre, A. et al. Case fatality rates of Ebola virus diseases: a meta-analysis of World Health Organization data. *Méd. et. Maladies Infect.* **44**, 412–416 (2014).
7. Kabami, Z. et al. Ebola disease outbreak caused by the Sudan virus in Uganda, 2022: a descriptive epidemiological study. *Lancet Glob. Health* **12**, e1684–e1692 (2024).
8. Ibrahim, S. K., Ndwandwe, D. E., Thomas, K., Sigfrid, L. & Norton, A. Sudan virus disease outbreak in Uganda: urgent research gaps. *BMJ Glob. Health* **7**, e010982 (2022).
9. Lee, J. E. et al. Structure of the Ebola virus glycoprotein bound to an antibody from a human survivor. *Nature* **454**, 177–182 (2008).

10. Harrison, S. C. Viral membrane fusion. *Nat. Struct. Mol. Biol.* **15**, 690–698 (2008).
11. Misasi, J. et al. Structural and molecular basis for Ebola virus neutralization by protective human antibodies. *Science* **351**, 1343–1346 (2016).
12. Saeed, M. F., Kolokoltsov, A. A., Albrecht, T. & Davey, R. A. Cellular entry of ebola virus involves uptake by a macropinocytosis-like mechanism and subsequent trafficking through early and late endosomes. *PLoS Pathog.* **6**, e1001110 (2010).
13. Chandran, K., Sullivan, N. J., Felbor, U., Whelan, S. P. & Cunningham, J. M. Endosomal proteolysis of the Ebola virus glycoprotein is necessary for infection. *Science* **308**, 1643–1645 (2005).
14. Carette, J. E. et al. Ebola virus entry requires the cholesterol transporter Niemann–Pick C1. *Nature* **477**, 340–343 (2011).
15. Gong, X. et al. Structural insights into the Niemann-Pick C1 (NPC1)-mediated cholesterol transfer and Ebola infection. *Cell* **165**, 1467–1478 (2016).
16. Wang, H. et al. Ebola viral glycoprotein bound to its endosomal receptor Niemann-Pick C1. *Cell* **164**, 258–268 (2016).
17. Gregory, S. M. et al. Structure and function of the complete internal fusion loop from Ebolavirus glycoprotein 2. *Proc. Natl. Acad. Sci.* **108**, 11211–11216 (2011).
18. Spence, J. S., Krause, T. B., Mittler, E., Jangra, R. K. & Chandran, K. Direct visualization of Ebola virus fusion triggering in the endocytic pathway. *MBio* **7**, 01857–01815 (2016).
19. Li, F. Receptor recognition mechanisms of coronaviruses: a decade of structural studies. *J. Virol.* **89**, 1954–1964 (2015).
20. Li, F. Structure, function, and evolution of coronavirus spike proteins. *Annu. Rev. Virol.* **3**, 237–261 (2016).
21. Shang, J. et al. Structural basis of receptor recognition by SARS-CoV-2. *Nature* **581**, 221–224 (2020).
22. Li, F., Li, W., Farzan, M. & Harrison, S. C. Structure of SARS coronavirus spike receptor-binding domain complexed with receptor. *Science* **309**, 1864–1868 (2005).
23. Ng, M. et al. Filovirus receptor NPC1 contributes to species-specific patterns of ebolavirus susceptibility in bats. *eLife* **4**, e11785 (2015).
24. Sigma-Aldrich. The human protein atlas. (2009).
25. Cantoni D., Hamlet A., Michaelis M., Wass M. N., Rossman J. S. Risks posed by Reston, the forgotten Ebolavirus. *mSphere* **1**, (2016).
26. Ye, G. et al. Structure-guided in vitro evolution of nanobodies targeting new viral variants. *PLoS Pathog.* **20**, e1012600 (2024).
27. Zhang, W. et al. Structural evolution of SARS-CoV-2 omicron in human receptor recognition. *J. Virol.* **97**, e0082223 (2023).
28. Ye, G. et al. Dual-role epitope on SARS-CoV-2 spike enhances and neutralizes viral entry across different variants. *PLoS Pathog.* **20**, e1012493 (2024).
29. Zhang, W. et al. Structural basis for mouse receptor recognition by bat SARS2-like coronaviruses. *Proc. Natl. Acad. Sci. USA* **121**, e2322600121 (2024).
30. Punjani, A., Rubinstein, J. L., Fleet, D. J. & Brubaker, M. A. cryoSPARC: algorithms for rapid unsupervised cryo-EM structure determination. *Nat. Methods* **14**, 290–296 (2017).
31. Rubinstein, J. L. & Brubaker, M. A. Alignment of cryo-EM movies of individual particles by optimization of image translations. *J. Struct. Biol.* **192**, 188–195 (2015).
32. Rohou, A. & Grigorieff, N. CTFFIND4: Fast and accurate defocus estimation from electron micrographs. *J. Struct. Biol.* **192**, 216–221 (2015).
33. Dai, X., Wu, L., Yoo, S. & Liu, Q. Integrating AlphaFold and deep learning for atomistic interpretation of cryo-EM maps. *Brief. Bioinforma.* **24**, bbad405 (2023).
34. Emsley, P. & Cowtan, K. Coot: model-building tools for molecular graphics. *Acta Crystallogr. Sect. D.-Biol. Crystallogr.* **60**, 2126–2132 (2004).
35. Adams, P. D. et al. PHENIX: a comprehensive Python-based system for macromolecular structure solution. *Acta Crystallogr. Sect. D.-Biol. Crystallogr.* **66**, 213–221 (2010).
36. Goddard, T. D. et al. UCSF ChimeraX: Meeting modern challenges in visualization and analysis. *Protein Sci.: Publ. Protein Soc.* **27**, 14–25 (2018).
37. DeLano, W. L. PyMOL: an open-source molecular graphics tool. *CCP4 Newsl. Protein Crystallogr* **40**, 82–92 (2002).
38. Laskowski, R. A. & Swindells, M. B. LigPlot+: multiple ligand-protein interaction diagrams for drug discovery. *J. Chem. Inf. Model* **51**, 2778–2786 (2011).

## Acknowledgements

This study was supported by funding from NIH grant U19AI171954 (to F.L. and B.L.). The Biacore S200 system was supported by NIH ORIP grant 1S10OD021539.

## Author contributions

F.B.: Conceptualization, Data curation, Investigation, Validation, Writing – review & editing; G.Y.: Conceptualization, Data curation, Formal analysis, Investigation, Validation, Writing – review & editing; H.T.H.: Investigation, Validation; M.H.: Investigation, Validation; B.L.: Data curation, Investigation, Validation, Writing – review & editing; F.L.: Conceptualization, Funding acquisition, Project administration, Supervision, Validation, Writing – original draft.

## Competing interests

The authors declare no competing interests.

## Additional information

**Supplementary information** The online version contains supplementary material available at https://doi.org/10.1038/s42003-025-07613-y.

**Correspondence** and requests for materials should be addressed to Bin Liu or Fang Li.

**Peer review information** *Communications Biology* thanks the anonymous reviewers for their contribution to the peer review of this work. Primary Handling Editors: Madlen Luckner and Laura Rodríguez Pérez.